eprints@whiterose.ac.uk
https://eprints.whiterose.ac.uk/

Theoretical Harmonic Spectra of PWM Waveforms Including DC Bus Voltage Ripple – Application to a Low-Capacitance Modular Multilevel Converter

Sumeet Singh Thakur, Milijana Odavic, *Member, IEEE*, Ahmed Allu, Z. Q. Zhu, *Fellow, IEEE,* and Kais Atallah

Abstract- **This paper develops a new closed-form analytical solution to the harmonic spectrum of the Pulse Width Modulated (PWM) output voltage of the single-phase inverter connected to the dc-bus with considerable voltage ripple. The solution is based on a double Fourier series expansion in two variables. As the single phase inverter forms the basic building block of most converters, the developed expressions can be applied to various topologies. This study first identifies the interactions of a single-frequency sinusoidal modulation signal and the carrier signal with the dc-bus voltage harmonics. The dc-bus voltage harmonics are constrained in this work to multiples of the inverter output voltage fundamental frequency. The analysis is then extended to include a multi-frequency modulation signal. Starting from the general solution, new expressions for the output voltage harmonics of the Modular Multilevel Converter (MMC) are developed. The low-capacitance MMC is chosen in this analysis due to inherent low-frequency voltage oscillations in the converter internal capacitors. The MMC analytical harmonic spectrum can incorporate the effects of the circulating current control and third harmonic injection PWM, by including the second and third order harmonic components in the modulation signal, respectively. The MMC analytical harmonic spectrum is benchmarked against the experimental results.**

Index Terms—PWM, harmonic spectrum, Fourier series, dc-bus voltage ripple, modular multilevel converter.

I. INTRODUCTION

Modern power converters need to follow strict power quality constraints [1], [2]. The harmonic content of PWM converters can be obtained by using a simulation package (such as Matlab) to create a PWM waveform and then analyze this by a Fast Fourier Transform (FFT). The major limitation of this approach is the necessity of a small simulation time step for any meaningful results. To overcome this, the analytical solutions for the harmonic components of the typical PWM converters have been developed [3-15]. A double Fourier series expansion in two variables is a well-established approach commonly used for the frequency-domain representation of a PWM waveform with a single-frequency sinusoidal modulation signal [3]–[7]. This approach has been also successfully employed to the more complex problems, such as the third harmonic injection PWM [7] and active filter applications [8], when the modulation signal includes fundamental and baseband components. The alternative methods to analyzing the PWM spectrum have been developed [9]–[15]. These are mostly based on a single Fourier series representation. In [14], the PWM spectrum analysis is extended

to non-periodic modulation waveforms and it was shown that superposition of modulation signals in the time-domain results in the convolution of the sideband harmonics in the frequency-domain. In [9], the elegant method of incorporating dead-time into a PWM waveform and the associated closed-form harmonic spectrum expressions are developed.

One of the assumptions usually made in analyzing the harmonic spectrum of the PWM inverter connected to the dc-bus is that the dc-bus voltage contains only a pure dc component. This assumption is typically justified for the dc-bus with high-frequency voltage ripple, as this can be easily suppressed. For the MMC applications, however, this assumption may not be valid. The MMC is composed of a cascade of identical Sub-Modules (SMs), which are characterized by inherent low-frequency voltage oscillations in their internal capacitors. This is due to the single-phase nature of the SMs, as each SM consists of a capacitor and a half-bridge converter [16]–[20]. These oscillations can be suppressed by increasing the capacitance of each SM, however, in the MMCs with a large number of SMs this may lead to an unacceptable increase in the cost and size of the system [21], [22].

Recent studies have shown that the low frequency voltage oscillations in the MMC can be increased without causing a significant increase in the peak voltage stress. This is due to the fact that the low frequency voltage oscillations, which are generally present in converter structures composed of a cascade of half-bridge or full-bridge converters, are of the first and second order, which in turn can be used to accommodate the increased modulation index under certain power factor conditions. This property has been utilized in the design of a low capacitance Cascaded H-Bridge converter for reactive power support [23]–[25]. A similar concept has been adopted for a low capacitance MMC [22], [26], [27]. Although the operation of the MMC under increased voltage ripple is demonstrated, the effects of such low frequency ripple on the harmonic spectrum are not well understood.

Some primarily studies concerning the effects of non-ideal dc-bus voltage can be found in the literature [28]–[30]. In [28], a feed-forward dc-bus voltage ripple compensation method for the multilevel inverters is proposed. The effects of this ripple on the output voltage are discussed concerning the baseband harmonics, however, no attention has been given to the high frequency harmonics. The authors in [29] present the mathematical expressions for the output voltage harmonic

spectrum of the Cascaded H-Bridge converter for StatCom applications, accounting for the second order harmonic in the internal capacitor voltages. However, the second harmonic in the capacitor voltages is only related to the Cascaded H-Bridge converters with the internal floating capacitors. The is not the case if this converter is fed by single-phase or three-phase diode rectifiers. Also, considering the other multilevel topologies such as the MMC, the capacitor voltage ripple is not limited to the second harmonic only. An improved Phase-Shifted Carrier (PSC) PWM is proposed in [30] to suppress the effects of the low-frequency capacitor voltage ripple in the MMC. The authors have successfully demonstrated the interactions of the low frequency SM capacitor voltage ripple and the second harmonic component in the modulation signal, caused by the circulating current control, leading to the additional low frequency harmonics in the output voltage of each SM. However, detailed analysis of these interactions and their effects on the high frequency spectrum are not provided.

This paper develops a new closed-form analytical solution to the output voltage harmonic spectrum of the single phase inverter connected to the dc bus with considerable voltage ripple. The dc bus voltage harmonics are however constrained in this analysis to multiples of the inverter output voltage fundamental frequency. Section-IIA includes the well-established expressions for the output voltage harmonics considering a pure dc component in the dc bus. The new solution is first developed considering a single-frequency sinusoidal modulation signal and arbitrary voltage harmonics in the dc bus, as presented in Section-IIB. The solution is further developed in Section-IIC by incorporating a multi-frequency modulation signal. The new solution can thus take into account the effects of the feedback control loops on the output voltage spectrum by including the additional harmonic components in the modulation signal. As the single phase inverter forms the basic building block of most converters, the developed solution can be applied to various topologies. This is demonstrated in Section III by developing the analytical harmonic spectrum of the MMC output voltage. The MMC harmonic solution can include the effects of the closed loop circulating current control by incorporating the second harmonic component in the modulation signal. The control of the second harmonic circulating current to zero is the important property of the MMC [19], [31], [32]. Also, the analysis includes the effects of the third order harmonic component in the modulation signal on the spectrum. The third harmonic injection PWM is typically used to increase the linear operation range of the converter [26], [33]. The MMC analytical harmonic spectrum is benchmarked
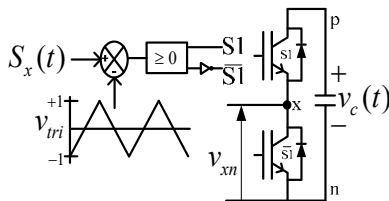
against the experimental results in Section IV. The effect of SM capacitor voltage ripple on the output filter requirements is discussed in Section V. The concluding remarks are given in Section VI.

II. A GENERAL ANALYTICAL SOLUTION TO THE HARMONIC SPECTRUM OF THE SINGLE PHASE INVERTER OUTPUT VOLTAGE

This section develops a general analytical solution to the output voltage harmonic spectrum of the single phase inverter connected to the dc-bus with considerable voltage harmonics. The single phase inverter and the associated double-edge carrier based PWM, which are assumed in this work, are shown in Fig.1. The sampling is considered to be natural for the sake of simplicity. The effects of the reference voltage sampling on the harmonic spectrum are however well understood and documented [5], [7]. The analysis is based on the double Fourier series expansion [7].

IIA. The harmonic spectrum considering a single-frequency modulation signal and ideal dc-bus voltage

The well-established analytic solution to the harmonic spectrum of the single phase inverter output voltage is included in this section for the sake of completeness. It assumes a pure dc component in the dc-bus voltage, denoted hereafter as V_c^0, and a single-frequency sinusoidal modulation signal, with amplitude M_1, given by:

$$S_x(t) = M_1 cos(y) \tag{1}$$

The analytical harmonic spectrum of the output voltage is [7]:

$$v_{xn}(t) = \frac{V_c^0}{2} + \frac{V_c^0}{2} M_1 \cos(y)$$
$$+ \sum_{m=1}^{\infty} \sum_{n=-\infty}^{\infty} \left[\frac{2V_c^0}{m\pi} J_n \left(mM_1 \frac{\pi}{2} \right) sin \left((m+n) \frac{\pi}{2} \right) \cos(ny + mz) \right] \tag{2}$$

where m and n represent multiples of the carrier and fundamental frequency, respectively. The variables y and z are defined by (3a) and (3b); where ω_o / θ_x and ω_c / θ_c are the fundamental and carrier frequency/phase shift angles, respectively. The expression $J_n(mM_1\pi/2)$ is an nth order Bessel function of the first kind whose argument is $(mM_1\pi/2)$. The coefficients of the double Fourier series expansion are obtained by solving (4), for the dc-bus voltage given by $v_c(t) = V_c^0$. The general form of the harmonic spectrum of a carrier-based PWM waveform is provided in (A0) in Appendix.

$$y = \omega_o t + \theta_x \tag{3a}$$
$$z = \omega_c t + \theta_c \tag{3b}$$
$$C_{m,n} = \frac{1}{2\pi^2} \int_{-\pi}^{\pi} \int_{-\frac{\pi}{2}(1+M_1 Cosy)}^{\frac{\pi}{2}(1+M_1 Cosy)} v_c(t) \, e^{j(mz+ny)} dz \, dy \tag{4}$$

IIB. The harmonic spectrum considering a single-frequency modulation signal and non-ideal dc-bus voltage

The dc-bus voltage harmonics considered in the work are constrained to multiples of the inverter output voltage

Fig. 1. Single phase inverter connected to the dc-bus (where S_x and V_{tri} denote the modulation and carrier signals respectively)

fundamental frequency. The dc-bus voltage can then be written in the following form:

$$v_c(t) = V_c^0 + V_c^{i_1} Cos\left(i_1 y + \theta_{h_{i_1}}\right) + V_c^{i_2} Cos\left(i_2 y + \theta_{h_{i_2}}\right) + \cdots \qquad (5)$$
$$= \sum_{i \in I} V_c^i Cos\left(iy + \theta_{h_i}\right)$$

where V_c^i is the amplitude and θ_{h_i} is the phase shift angle (with respect to the reference output voltage) of the ith order harmonic in the dc-bus voltage. Here, $i \in I$ and $I = \{0, i_1, i_2, i_3, ..\}$, where $(i_1, i_2, i_3, ...)$ are natural numbers and $\theta_{h_0} = 0$. The coefficients of the double Fourier series of the output voltage, with the dc-bus voltage defined by (5) and the modulation signal defined by (1), can be obtained by:

$$C_{m,n} = C_{m,n}^0 + C_{m,n}^{i_1} + C_{m,n}^{i_2} + \cdots = \sum_{i \in I} C_{m,n}^i \qquad (6)$$

where

$$C_{m,n}^i = \frac{1}{2\pi^2} \int_{-\pi}^{\pi} \int_{-\frac{\pi}{2}(1+M_1 Cosy)}^{\frac{\pi}{2}(1+M_1 Cosy)} V_c^i Cos\left(iy + \theta_{h_i}\right) e^{j(mz+ny)} dx \, dy. \qquad (7)$$

Therefore, by solving (7) for each harmonic in the dc-bus voltage separately and then applying (6), the total solution can be obtained and is given by (8), where the terms in the summations are added for any values of i, K and u_1 for which the particular conditions are fulfilled (with $I = \{0, i_1, i_2, ..\}, 0 \le K \le \infty$ and $u_1 = \{1, -1\}$). For example, term ($V_c^i e^{-j\theta_{h_i}}/2$) in (8b) is non-zero if $n = i$, otherwise is zero.

$$v_{xn}(t) = \frac{V_c^0}{2} + \sum_{\substack{i \in I \\ i \ne 0}} \frac{M_1 V_c^i}{4} cos(\theta_{h_i}) \Big|_{i=1} \qquad (8a)$$

$$+ \frac{M_1 V_c^0}{2} Cos(y) \qquad (8b)$$

$$+ Re \sum_{n=1}^{\infty} \left(\left\{ \sum_{\substack{i \in I \\ i \ne 0}} \left[\frac{V_c^i}{2} e^{-j\theta_{h_i}} \Big|_{n=i} + \frac{M_1 V_c^i}{4} e^{-j\theta_{h_i}} \Big|_{n=|1\pm i|} \right] \right\} e^{-jny} \right)$$

$$+ Re \sum_{m=1}^{\infty} \sum_{n=-\infty}^{\infty} \left(\left\{ \sum_{i \in I} \sum_{K, u_1} \frac{V_c^i}{\pi m} \left\{ e^{-j\left(u_1 \theta_{h_i}\right)} J_K \left(m M_1 \frac{\pi}{2} \right) Sin \left((m + K) \frac{\pi}{2} \right) \right\} \Big|_{n=iu_1 \pm K} \right\} \cdot e^{-j(mz+ny)} \right) \qquad (8c)$$

Based on the expressions (8a)-(8c), the conclusions can be drawn to summarize the effects of the dc-bus voltage harmonics on the output voltage harmonic spectrum. In general, the ith order harmonic in the dc bus voltage will generate the baseband harmonics of the order $n = i$ and $n = \|1 \pm i\|$, as can be seen from (8b). The ith order harmonic in the dc bus voltage will also generate the carrier and sideband harmonics of the order $n = (\pm i \pm K)$ with $K = (0, 2, 4, ...)$ for the odd carrier groups and $K = (1, 3, 5, ...)$ for the even carrier groups, as can be seen from (8c). The dc component in the harmonic spectrum can be affected only by the first harmonic in the dc-bus voltage, as the term $\{M_1 V_c^i cos(\theta_{h_i})/4\}$ in (8a) is non zero when $i = 1$. The fundamental component can be affected by the first and second
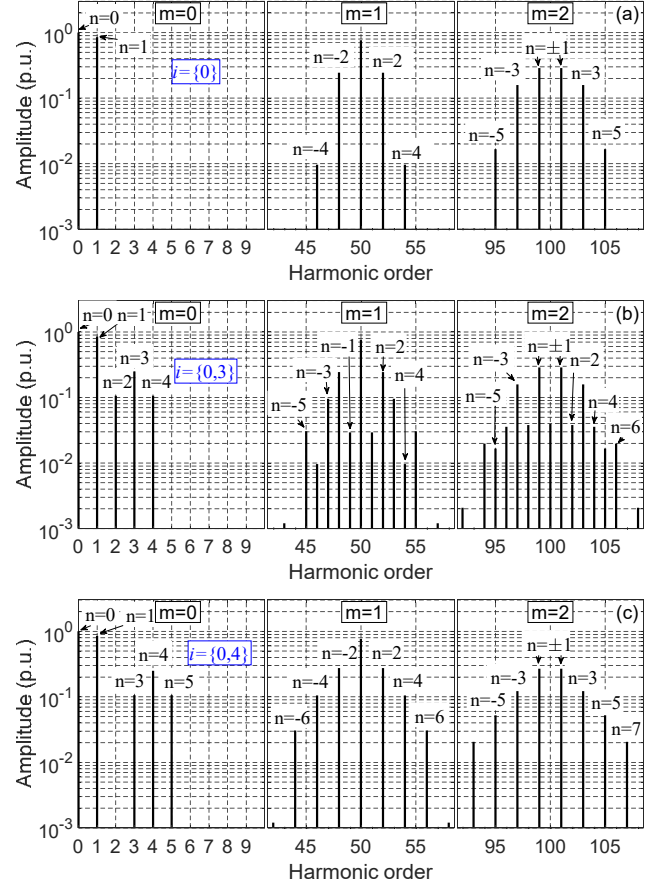

Fig. 2. Analytical harmonic spectrum (Eq. (8)): (a) $i = 0$. (b) $i = \{0,3\}$. (c) $i = \{0,4\}$. System variables: $V_c^0 = 1, V_c^3 = 0.25, \theta_{h_3} = 0, V_c^4 = 0.25$, $\theta_{h_4} = 0, M_1 = 0.85, \omega_c/\omega_o = 50$. ('$i$' is the order of the harmonics in the dc bus voltage).

order harmonics in the dc-bus voltage, as can be seen from (8b) for $n = 1$.

The differences in the harmonic distribution of the output voltage for the odd and even harmonics in the dc bus voltage can be clearly seen in Fig.2. Firstly, Fig.2(a) shows the analytical harmonic spectrum of the inverter output voltage for the pure dc component in the dc bus voltage, i.e. for $i = 0$. As expected, there are no other harmonics in the baseband frequency range, only the fundamental and dc components are present. Also, the even sidebands are present in the first carrier group ($m = 1$), and the odd sidebands in the second carrier group ($m = 2$). Fig.2(b) then presents the harmonic spectrum of the output voltage when the dc bus voltage contains the dc and odd order harmonic component, i.e. $i = \{0,3\}$. The harmonics of the order $n = 3$ and $n = \|1 \pm 3\|$ can be clearly identified in the baseband frequency range. Also, in the first carrier group, in addition to the sidebands that are already present for $i = 0$, the odd order sidebands also appear. Similarly, both the even and odd order sideband harmonics are present in the second carrier group. Further, Fig.2(c) shows the case when the dc bus voltage contains the even harmonic component, i.e. $i = \{0,4\}$. In this case no additional harmonics
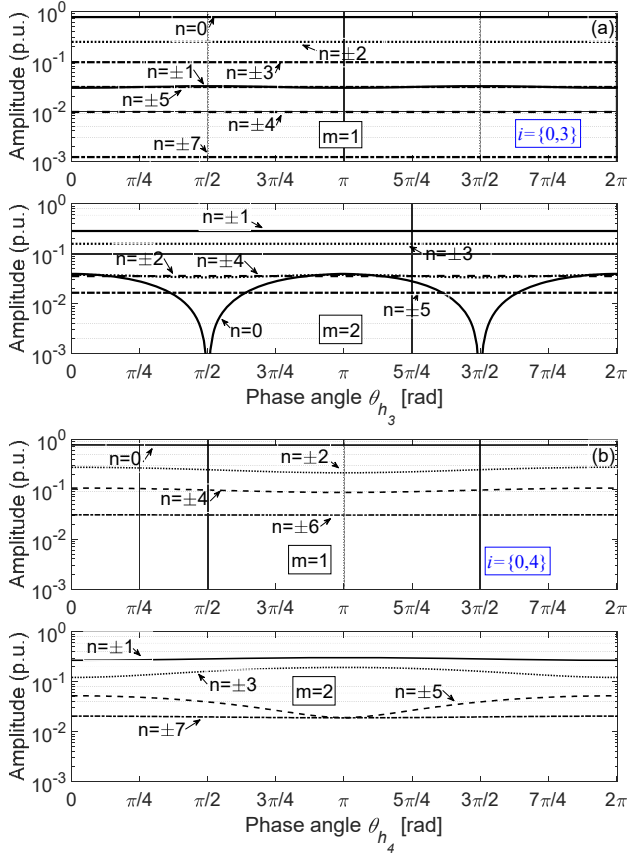
Fig. 3. Harmonics in the first (m=1) and second (m=2) carrier groups (Eq. (8)) versus the phase shift angle of the dc bus voltage harmonic for: (a) $i =$ $\{0,3\}$. (b) $i = \{0,4\}$. System variables: $V_c^0 = 1, V_c^3 = 0.25, V_c^4 = 0.25$, $M_1 = 0.85, \omega_c/\omega_o = 50$.

are generated in the first and second carrier groups, however, the amplitudes of the sidebands, which are already present for $i = 0$, are affected. In the baseband frequency range, as expected, the harmonics of the order $n = 4$ and $n = \|1 \pm 4\|$ are generated.

Fig.3 demonstrates the nonlinear behaviour of the sideband harmonics in the harmonic spectrum when the phase shift angle of the dc-bus voltage harmonic is varying in the range from zero to 2π. Fig.3(a) shows the sidebands of the first ($m = 1$) and second ($m = 2$) carrier groups when the dc bus voltage contains the third harmonic component (i.e. $i = \{0,3\}$). Fig.3(b) shows the sidebands of the first and second carrier groups for $i = \{0,4\}$.

The analytical solution (8) is evaluated against the simulation results for $i = \{0,1,2,6\}$, as shown in Fig.4(b). The simulation results are obtained by applying the FFT analysis on the output voltage waveform obtained from the inverter switching model developed in Matlab/Simulink. The developed solution (8) is in excellent agreement with the simulation results. For comparison purposes, the classical solution (2) [7] is also compared against the simulation results, as shown in Fig.4(a).
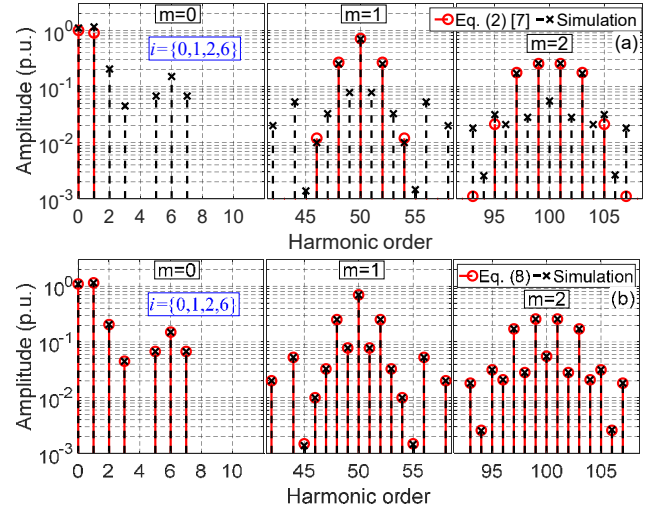

Fig. 4. Simulation against analytical results $i = \{0,1,2,6\}$. (a) Eq. (2) [7]. (b) Eq. (8). System variables: $V_c^0 = 1, V_c^1 = 0.25, \theta_{h_1} = \frac{\pi}{6}, V_c^2 = 0.1, \theta_{h_2} = \frac{\pi}{3}, V_c^6 = 0.1, \theta_{h_6} = -\frac{\pi}{2}, M_1 = 0.9, \omega_c/\omega_o = 50$.

IIC. The harmonic spectrum considering a multi-frequency modulation signal and non-ideal dc-bus voltage

The analytical harmonic spectrum of the inverter output voltage with a modulation signal, which includes fundamental and two additional arbitrary harmonic components, as given by (9), is derived in this section. Hereafter, the variable p is introduced, which represents the order of the harmonics in the modulation signal. In (9), $p = \{1, p_2, p_3\}$ and θ_{p_2} and θ_{p_3} are the phase shift angles of the p_2^{th} and p_3^{th} order harmonic components, respectively.

$$S_x(t) = M_1 \cos(y) + M_{p_2} \cos(p_2 y + \theta_{p_2}) + M_{p_3} \cos(p_3 y + \theta_{p_3}) \quad (9)$$

The coefficients of the double Fourier series, with the dc-bus voltage defined by (5) and the modulation signal defined by (9), can be obtained by (A1a)-(A1b), as given in Appendix. After solving (A1b) for each harmonic in the dc bus voltage separately, and then applying (A1a), the total solution can be obtained as given by (10) where the terms in the summations are added for any values of i, u_1, u_2, u_3, K, H and Z for which the particular conditions are fulfilled (where $I = \{0, i_1, i_2, ..\}$, $0 \le K \le \infty$, $0 \le H \le \infty$, $0 \le Z \le \infty$, $u = \{1, -1\}$, $u_1 = \{1, -1\}$, $u_2 = \{1, -1\}$ and $u_3 = \{1, -1\}$). It should be noted that due to the rapid roll-off of the Bessel functions values, it is sufficient to consider the summation over the first 10 terms of K, H and Z i.e., $0 \le K \le 10, 0 \le H \le 10, 0 \le Z \le 10$ [7]. From (10), the interactions between the ith order harmonic in the dc bus voltage and the pth order harmonic in the modulation signal and their effects on the inverter output voltage harmonic spectrum can be clearly identified. In general, the ith order harmonic in the dc bus voltage will generate the baseband harmonics of the order $n = i$, $n = \|1 \pm i\|$, $n = \|p_2 \pm i\|$ and
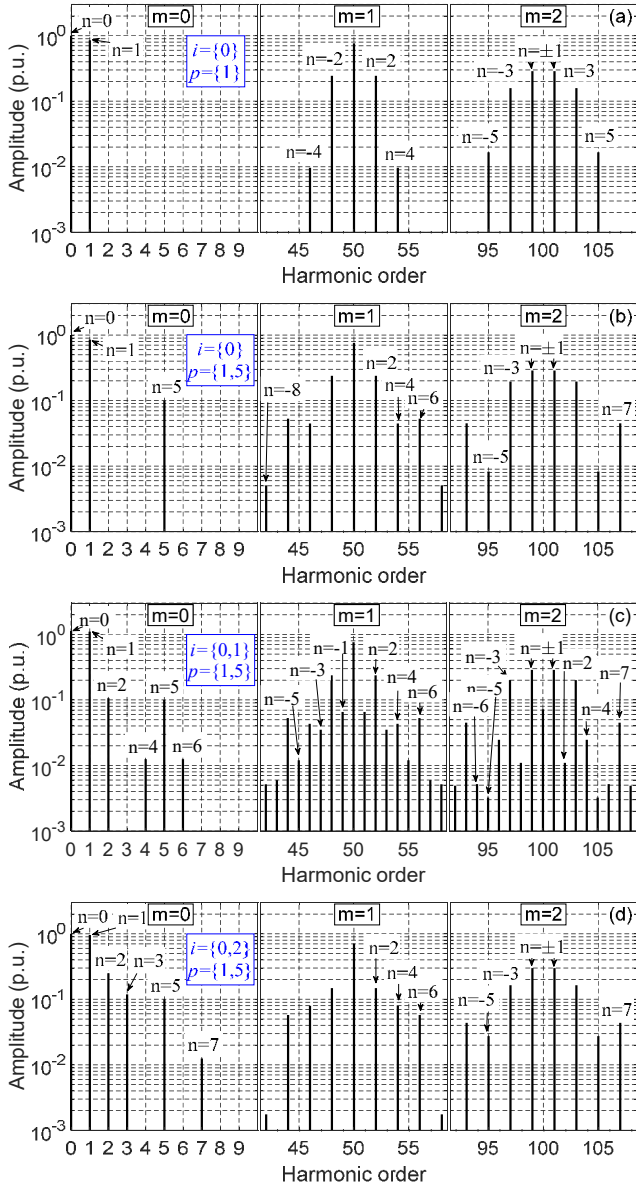
Fig. 5. Analytical harmonic distribution (Eq. (10)) for (a) $i = 0$; $p = 1$. (b) $i = 0$; $p = \{1,5\}$. (c) $i = \{0,1\}$; $p = \{1,5\}$. (d) $i = \{0,2\}$; $p = \{1,5\}$. System variables: $V_c^0 = 1, V_c^1 = 0.25, V_c^2 = 0.25, M_1 = 0.85, M_5 = 0.1, \theta_{h_1} = \theta_{h_2} = \theta_5 = 0, \omega_c/\omega_o = 50$.

$n = \|p_3 \pm i\|$, as can be seen from (10b). Also, the ith order harmonic in the dc bus voltage will generate the carrier and sideband harmonics of the order $n = (\pm i \pm K \pm p_2 H \pm p_3 Z)$ for $(m + K + H + Z)$ is odd, as is revealed by expression (10c). Finally, the ith order harmonic in the dc bus voltage can also affect the dc component of the output voltage, when the condition of $p = i$ is fulfilled, as can be seen from (10a).

The effects of the odd/even harmonic in the dc bus voltage on the harmonic distribution of the output voltage with the multi-frequency modulation signal can be seen in Fig.5. The results in Fig.5 are obtained by the analytical expressions (10) for different (i, p) combinations. For comparison purposes, Fig.5(a) shows the analytical harmonic spectrum for the pure dc component in the dc-bus voltage and only the fundamental component in the modulation signal (i.e. $i = 0$ and $p = 1$). Fig.5(b) then shows the harmonic spectrum with the additional component in the modulation signal (i.e. for $i = 0$ and $p = \{1,5\}$). In comparison with Fig.5(a), the harmonic spectrum is redistributed with significant harmonics up to the 8th sidebands for the first carrier group. The harmonic spectrum for the first harmonic in the dc bus voltage and the fundamental and fifth harmonic components in the modulation signal (i.e. for $i = \{0,1\}$ and $p = \{1,5\}$), is shown in Fig.5(c). Here, the new baseband harmonics of the order $n = i$ and $n = \|1 \pm 1\|$ and $n = \|5 \pm 1\|$ can be identified. Also, the additional odd order sideband harmonics, of the order $n = (\pm 1 \pm K \pm 5H)$ for $(K + H)$ is even, are present in the first carrier group. While, the additional even order sideband harmonics, of the order $n = (\pm 1 \pm K \pm 5H)$ for $(K + H)$ is odd, are present in the second carrier group. Finally, the harmonic spectrum for $i = \{0,2\}$ and $p = \{1,5\}$ is shown in Fig.5(d). It can be seen that no additional sidebands have been generated, in comparison with Fig.5(b), however, the even harmonic in the dc bus voltage will affect the sideband harmonics amplitudes.

The analytical solution (10) is evaluated against the simulation results for $i = \{0,2,6\}$ and $p = \{1,3,5\}$ as shown in Fig.6(c). The simulation results are obtained by applying the FFT analysis on the output voltage waveform obtained from the inverter switching model developed in Matlab/Simulink. The developed solution (10) is in excellent agreement with the simulation results. For comparison purposes, the classical

$$v_{xn}(t) = \frac{V_c^0}{2} + \sum_{\substack{i \in I \\ i \neq 0}} \left(\left. \frac{V_c^i}{4} M_1 Cos(\theta_{h_i}) \right|_{i=1} + \left. \frac{V_c^i}{4} M_{p_2} Cos(\theta_{h_i} - \theta_{p_2}) \right|_{i=p_2} + \left. \frac{V_c^i}{4} M_{p_3} Cos(\theta_{h_i} - \theta_{p_3}) \right|_{i=p_3} \right) \tag{10a}$$

$$+ \frac{M_1 V_c^0}{2} Cos(y) + \frac{M_{p_2} V_c^0}{2} Cos(p_2 y + \theta_{p_2}) + \frac{M_{p_3} V_c^0}{2} Cos(p_3 y + \theta_{p_3}) \tag{10b}$$

$$+ Re \sum_{n=1}^{\infty} \left(\left\{ \sum_{\substack{i \in I \\ i \neq 0}} \left. \frac{V_c^i}{2} e^{-j\theta_{h_i}} \right|_{n-i=0} + \sum_{u=-1,1} \left(\left. \frac{V_c^i}{4} M_1 e^{-j\theta_{h_i}} \right|_{n=|1\pm i|} + \left. \frac{V_c^i}{4} M_{p_2} e^{-ju(\theta_{h_i} - \theta_{p_2})} \right|_{n=u(i-p_2)} + \left. \frac{V_c^i}{4} M_{p_2} e^{-j(\theta_{h_i} + \theta_{p_2})} \right|_{n=i+p_2} + \left. \frac{V_c^i}{4} M_{p_3} e^{-ju(\theta_{h_i} - \theta_{p_3})} \right|_{n=u(i-p_3)} + \left. \frac{V_c^i}{4} M_{p_3} e^{-j(\theta_{h_i} + \theta_{p_3})} \right|_{n=i+p_3} \right) \right] \right\} e^{-jny} \right) \tag{10c-upper}$$

$$+ Re \sum_{m=1}^{\infty} \sum_{n=-\infty}^{\infty} \left(\left\{ \sum_{i \in I} \left[\sum_{\substack{u_1,u_2,u_3, \\ K,H,Z}} \frac{V_c^i}{\pi m} \left\{ e^{-j(u_1 \theta_{h_i} + u_2 H \theta_{p_2} + u_3 Z \theta_{p_3})} J_K\left(mM_1 \frac{\pi}{2}\right) J_H\left(mM_{p_2} \frac{\pi}{2}\right) J_Z\left(mM_{p_3} \frac{\pi}{2}\right) \cdot \right. \right. \right. \right. \right. \left. \left. \left. Sin\left((m + K + H + Z)\frac{\pi}{2}\right) \right\} \right]_{n=u_1 i \pm K + u_2 p_2 H + u_3 p_3 Z} \right\} e^{-j(mz+ny)} \right) \tag{10c}$$
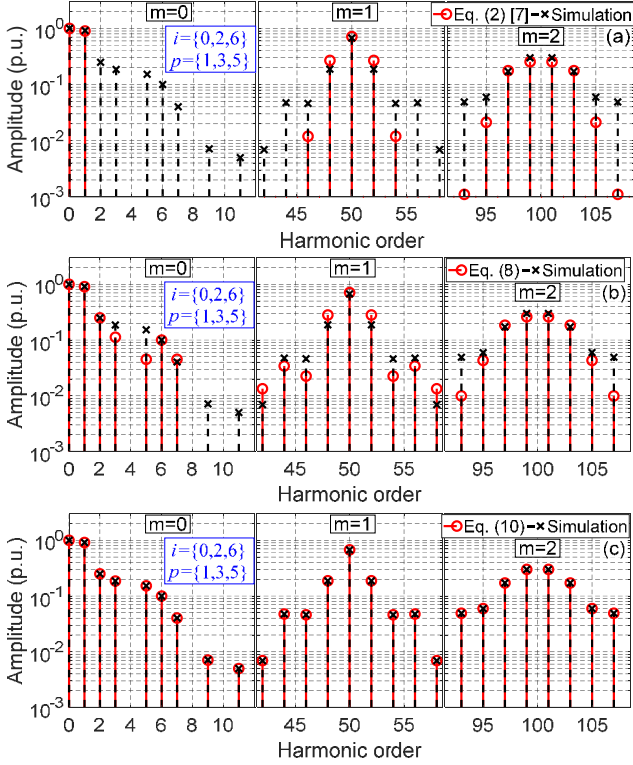
Fig. 6. Simulation against analytical results $i = \{0,2,6\}$; $p = \{1,3,5\}$. (a) Eq. (2) [7]. (b) Eq. (8). (c) Eq. (10). System variables: $V_c^0 = 1, V_c^2 = 0.25$, $\theta_{h_2} = -\frac{\pi}{2}, V_c^6 = 0.1, \theta_{h_6} = -\frac{\pi}{3}, M_1 = 0.9, p_2 = 3, M_3 = -0.142, \theta_3 = 0, p_3 = 5, M_5 = 0.1, \theta_5 = \frac{\pi}{6}, \omega_c/\omega_o = 50$.

solution (2) [7] is compared in Fig.6(a) and also the analytical model (8) is compared in Fig.6(b).

III. APPLICATION TO LOW CAPACITANCE MMC

IIIA. Mathematical modelling of MMC

The basic block diagram of the three-phase MMC is shown in Fig. 7. The converter consists of three legs, with each leg composed of two arms (upper and lower); where each arm is a series connection of N identical SMs and an inductor L_b. Each SM consists of a capacitor C and a half-bridge converter. The upper arm variables are represented by superscript 'u' and the lower arm variables are represented by superscript 'l'. The subscripts 'a,' b' and 'c' represent the three phases of the system. The three upper arm voltages are represented by v_x^u and the three lower arm voltages are represented by v_x^l where $x = \{a, b, c\}$. The three upper arm currents are i_x^u and the three lower arm currents are i_x^l. The output voltages are represented by v_{xo} and output currents by i_x. The net arm resistance is represented by R_b. The voltage and current at the dc terminals are E and i_{dc}, respectively. The capacitor voltage of the kth SM in the upper arm is represented as $v_{c,x}^{u,k}$ (k= 1,2,3..N) and in the lower arm as $v_{c,x}^{l,k}$ for k^{th} ($k = 1,2,3..N$). The output voltage of the kth SM in the upper arm is represented as $v_x^{u,k}$ and in the lower arm as $v_x^{l,k}$.
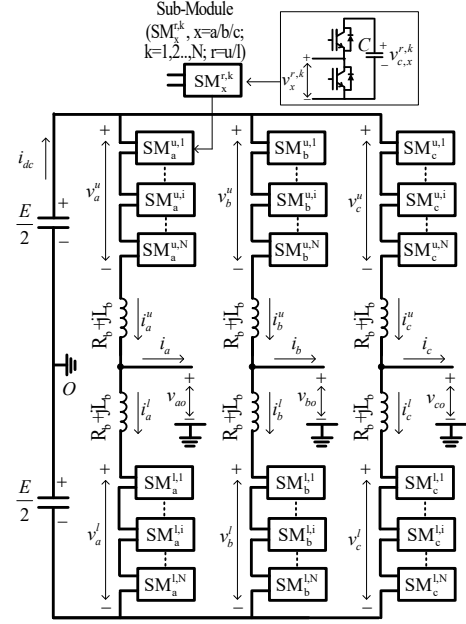

Fig. 7. Block diagram of a three-phase MMC.

The Phase Shifted Carrier (PSC) PWM is adopted in this work [34], [35]. In general, for an MMC with N SMs per arm, a total of $2N$ triangular carrier signals and $2N$ modulation signals are employed per leg; as a specific modulation signal and a carrier signal are assigned to each SM. The N carriers of each arm are shifted by $2\pi/N$ incrementally to achieve the optimal harmonics cancellation, resulting in the first sideband harmonics of the arm voltage harmonic spectrum centered about Nf_c (where f_c is the carrier frequency). As the carrier frequency determines the SM switching frequency, it is kept the same for all SMs. Also, the N carriers of the upper arm are shifted by θ_{psc} with respect to the N carriers of the lower arm, where $\theta_{psc} = 0$ for N is odd and $\theta_{psc} = \pi/N$ for N is even to maximize the harmonics cancellation, resulting in the output voltage harmonic spectrum with first sidebands centered about $2Nf_c$ [34]. In general, the phase shift angle of the kth SM carrier in the upper arm is $\theta_c^{u,k} = \theta_{psc} + \frac{2\pi}{N}(k-1)$ and in the lower arm is $\theta_c^{l,k} = \frac{2\pi}{N}(k-1)$.

The voltage balancing of the SM capacitors is typically achieved by adding a small dc component into the modulation signal of each SM [34]. As this value is normally very small it is neglected in this work. The modulation signal for each SM in the upper arm can then be considered to be the same and is given by (11a). Similarly, the modulation signal for each SM in the lower arm is given (11b).

$$M_a^{u,k} = M_1 Cos(\omega_o t + \pi) + M_2 Cos(2\omega_o t + \theta_2) + M_3 Cos(3\omega_o t) \quad (11a)$$
$$M_a^{l,k} = M_1 Cos(\omega_o t) + M_2 Cos(2\omega_o t + \theta_2) + M_3 Cos(3\omega_o t + \pi) \quad (11b)$$

The fundamental component in (11a) and (11b), with amplitude M_1 and frequency ω_o, controls the fundamental component of the output voltage. The second harmonic component in (11a) and (11b), with amplitude M_2 and frequency $2\omega_o$, controls the second harmonic circulating current (by means of the

circulating current controllers [31], [36]). The third harmonic component in (11a) and (11b), with amplitude M_3 and frequency $3\omega_o$, extends the linear operating range of the converter. The third harmonic injection PWM with $M_3 = M_1/6$ [26] is adopted in this work.

The capacitor voltage of each SM in the upper arm can be described by (12a) and in the lower arm by (12b). These expressions are the first order approximations of the square root of the arm energies [37]. The third and fourth order harmonic components in the capacitor voltage are neglected for simplicity. The amplitude V_c^1 and phase shift angle θ_{h_1} (with respect to the output reference voltage) of the first harmonic ($i_1 = 1$) in the capacitor voltage are given by (12c) and (12d), respectively. The amplitude V_c^2 and phase shift angle θ_{h_2} (with respect to the output reference voltage) of the second harmonic ($i_2 = 2$) in the capacitor voltage are given by (12e) and (12f), respectively. In (12c)-(12f), I_m, V_m, E and I_{dc} represent respectively the amplitudes of the output current, output voltage, input dc voltage and input dc current, and ϕ is the load angle.

$$v_{c,a}^{u,k}(t) = V_c^0 + V_c^1 Cos(\omega_o t + \theta_{h_1} + \pi) + V_c^2 Cos(2\omega_o t + \theta_{h_2}) \quad (12a)$$

$$v_{c,a}^{l,k}(t) = V_c^0 + V_c^1 Cos(\omega_o t + \theta_{h_1}) + V_c^2 Cos(2\omega_o t + \theta_{h_2}) \quad (12b)$$

$$V_c^1 = \frac{1}{NCV_c^0}\sqrt{\left(\frac{EI_m}{4\omega_o}\right)^2 + \left(\frac{V_m I_{dc}}{3\omega_o}\right)^2 - 2\frac{EI_m}{4\omega}\frac{V_m I_{dc}}{3\omega_o}Cos(\phi)} \quad (12c)$$

$$\theta_{h_1} = -\frac{\pi}{2} + atan\left(\frac{-\frac{EI_m}{4\omega_o}Sin(\phi)}{\frac{V_m I_{dc}}{3\omega_o} - \frac{EI_m}{4\omega_o}Cos(\phi)}\right) \quad (12d)$$

$$V_c^2 = \frac{V_m I_m}{8\omega_o NCV_c^0} \quad (12e)$$

$$\theta_{h_2} = \frac{\pi}{2} + \phi \quad (12f)$$

III.B The harmonic spectrum considering a single-frequency modulation signal and ideal dc-bus voltage

The analytical expressions for the harmonic characterization of the MMC, which are developed in [34], are included in this section for the sake of completeness. These expressions assume a pure dc component in the SM capacitor voltage (denoted as V_c^0), and a single-frequency sinusoidal modulation signal. These assumptions are justified if the MMC is operated without circulating current control [18]–[20] and with low SM capacitor voltage ripple. The output voltage of the kth SM in the upper and lower arms are given by (13a) and (13b), respectively.

$$v_a^{u,k}(t) = \frac{V_c^0}{2} - \frac{M_1 V_c^0}{2}Cos(\omega_o t) \quad (13a)$$

$$+ \sum_{m=1}^{\infty}\sum_{n=-\infty}^{\infty}\left[\begin{array}{c} \frac{2V_c^0}{m\pi}J_n\left(mM_1\frac{\pi}{2}\right)Sin\left((m+n)\frac{\pi}{2}\right). \\ Cos\left(m\left(\omega_c t + \frac{2\pi}{N}(k-1) + \theta_{psc}\right) + n(\omega_o t + \pi)\right) \end{array}\right]$$

$$v_a^{l,k}(t) = \frac{V_c^0}{2} + \frac{M_1 V_c^0}{2}Cos(\omega_o t) \quad (13b)$$

$$+ \sum_{m=1}^{\infty}\sum_{n=-\infty}^{\infty}\left[\begin{array}{c} \frac{2V_c^0}{m\pi}J_n\left(mM_1\frac{\pi}{2}\right)Sin\left((m+n)\frac{\pi}{2}\right). \\ Cos\left(m\left(\omega_c t + \frac{2\pi}{N}(k-1)\right) + n\omega_o t\right) \end{array}\right]$$

The upper arm and the lower arm voltages are given by:

$$v_a^u(t) = \frac{NV_c^0}{2} - \frac{NM_1 V_c^0}{2}Cos(\omega_o t) \quad (14a)$$

$$+ \sum_{m=1}^{\infty}\sum_{n=-\infty}^{\infty}\left[\begin{array}{c} \frac{2V_c^0}{m\pi}J_n\left(mNM_1\frac{\pi}{2}\right)Sin\left((mN+n)\frac{\pi}{2}\right). \\ Cos\left(mN(\omega_c t + \theta_{psc}) + n(\omega_o t + \pi)\right) \end{array}\right]$$

$$v_a^l(t) = \frac{NV_c^0}{2} + \frac{NM_1 V_c^0}{2}Cos(\omega_o t) \quad (14b)$$

$$+ \sum_{m=1}^{\infty}\sum_{n=-\infty}^{\infty}\left[\begin{array}{c} \frac{2V_c^0}{m\pi}J_n\left(mNM_1\frac{\pi}{2}\right)Sin\left((mN+n)\frac{\pi}{2}\right). \\ Cos(mN\omega_c t + n\omega_o t) \end{array}\right]$$

The output phase voltage is:

$$v_{ao}^-(t) = \frac{NM_1 V_c^0}{2}Cos(\omega_o t)$$

$$+ \sum_{m=1}^{\infty}\sum_{n=-\infty}^{\infty}\left[\begin{array}{c} \frac{2V_c^0}{m\pi}J_n\left(mNM_1\frac{\pi}{2}\right)Sin\left((mN+n)\frac{\pi}{2}\right). \\ Sin\left(mN\omega_c t + n\omega_o t + \frac{mN\theta_{psc} + n\pi}{2}\right). \\ Sin\left(\frac{mN\theta_{psc} + n\pi}{2}\right) \end{array}\right] \quad (15)$$

III.C The harmonic spectrum considering a multi-frequency modulation signal and non-ideal dc-bus voltage

Considering the low-capacitance MMC applications [22], [26], the new solution to the MMC output voltage harmonic spectrum is developed in this section. The general solution (10), developed in Section-IIC, is used first to obtain the analytical harmonic spectrum of the output voltage of the kth SM in the converter arms. By inspection of (11) and (3a), the phase shift angle of the fundamental component of the modulation signal of the upper arm is given as $\theta_x = \pi$. As required, the corresponding phase shift angle of the lower arm is then set to $\theta_x = 0$. By further inspection of (11) and (9): $M_{p_2} = M_2$, $p_2 = 2$, $\theta_{p_2} = \theta_2$, $M_{p_3} = M_3$, $p_3 = 3$, and $\theta_{p_3} = \pi$. The new solution for the output voltage harmonic spectrum of the kth SM in the upper arm can then readily be obtained from (10) and is given by (16a). Similarly, the solution for the output voltage harmonic spectrum of the kth SM in the lower arm can be obtained and is given by (16b). The upper and lower arm voltages can be obtained by the summation of the output voltages of all the SMs in the upper and lower arms, respectively, (i.e. $v_a^u = \sum_{k=1}^{N} v_a^{u.k}$ and $v_a^l = \sum_{k=1}^{N} v_a^{l.k}$). When the N carriers of each arm are shifted by $2\pi/N$ incrementally, the optimal solution for the harmonic distribution of the upper and lower arm voltages are given by (17a) and (17b), respectively. Finally, the new solution for the harmonic spectrum of the MMC output voltage, in which the effect of the
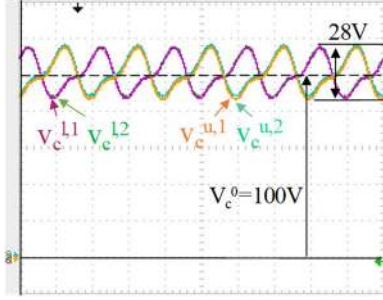
Fig. 8 Experimental results for SM capacitor voltages $v_{c,a}^{u,1}$, $v_{c,a}^{u,2}$, $v_{c,a}^{l,1}$ & $v_{c,a}^{l,2}$ [20V/div]. timescale: 10ms/div.

arm inductances is discarded (i.e. $v_{ao}^{-} = (v_a^l - v_a^u)/2$), is given by (18).

IV. EXPERIMENTAL VALIDATION

A single-phase MMC prototype consisting of two SMs per arm (*N*=2) is developed. The intelligent power module IKCM20L60GDXKMA1 from INFINEON is used for the custom designed printed circuit board SM. OPAL-RT 5607 is used as the control platform. The experimental setup parameters are given as: fundamental frequency of 50Hz, switching frequency of 2500Hz, input dc voltage E of 200V, arm inductance L_b of 2.9mH, phase shift angle θ_{psc} of $\pi/2$ and output voltage sampling time of 2μs. The single phase MMC feeds a resistive-inductive load (5.2Ω/1.86mH). The SM capacitance of $C = 660uF$ is used to demonstrate the effect of capacitor voltage ripple.

The MMC output voltage is controlled in open loop with $M_1 = 0.95$. The voltage balancing of the SM capacitors is

implemented as in [38], [39]. The steady-state capacitor voltages are shown in Fig. 8. The four SM capacitor voltages $v_{c,a}^{u,1}$, $v_{c,a}^{u,2}$, $v_{c,a}^{l,1}$ and $v_{c,a}^{l,1}$ are actively balanced, with the dc capacitor voltage of 100V and the peak-peak capacitor voltage ripple of 28V. A Proportional Resonant (PR) controller is used to control the second order harmonic of the circulating current to zero, as in [40]. The circulating current control injects the second harmonic component in the modulation signal. The third harmonic injection PWM with $M_3 = M_1/6$ is also implemented. The experimentally results without the third harmonic injection in the modulation signal (Case A) are presented first, as shown in Fig.9-Fig.11. Then the experimental results with the third harmonic injection (Case B) are shown in Fig.12. The steady state parameters for Case A are given as: $V_c^0 = 100V$, $V_c^1 = 10.8V$, $\theta_{h_1} = 86.4°$, $V_c^2 = 4.76V$, $\theta_{h_2} = 98.9°$, $M_1 = 0.95$, $M_2 = 0.1$, $\theta_2 = -83°$ and $M_3 = 0$. The steady state parameters for Case B are given as: $V_c^0 = 100V$, $V_c^1 = 10.8V$, $\theta_{h_1} = 84.25°$, $V_c^2 = 3.46V$, $\theta_{h_2} = 105°$, $M_1 = 0.95$, $M_2 = 0.092$, $\theta_2 = -82.22°$ and $M_3 = 0.1583$.

In Fig.9(a)-(c) the analytical solutions (13) and (16) are compared with the experimental results. Fig.9(a) shows the analytical harmonic spectrum (13) [34] in which the effects of the capacitor voltage ripple and circulating current control are neglected. The results clearly show that the third harmonic in the baseband frequency range and the odd/even sideband harmonics in the first/second carrier group are not accounted for. Fig.9(b) shows the analytical harmonic spectrum (16) in which variables i and p are set as $i = \{0,1,2\}$ and $p = 1$; in that, it includes the effects of the capacitor voltage ripple. The results show the second and third harmonics in the baseband frequency range which are caused by the interactions of the

$$v_a^{u,k}(t) = \frac{V_c^0}{2} + \frac{M_1 V_c^1}{4}Cos(\theta_{h_1}) + \frac{M_2 V_c^2}{4}Cos(\theta_{h_2} - \theta_2) + \tag{16a}$$
$$-\frac{M_1 V_c^0}{2}Cos(\omega_o t) - \frac{V_c^1}{2}Cos(\omega_o t + \theta_{h_1}) - \frac{M_1 V_c^2}{4}Cos(\omega_o t + \theta_{h_2}) - \frac{M_2 V_c^1}{4}Cos(\omega_o t + \theta_2 - \theta_{h_1}) + \frac{M_3 V_c^2}{4}Cos(\omega_o t - \theta_{h_2})$$
$$+\frac{M_2 V_c^0}{2}Cos(2\omega_o t + \theta_2) + \frac{V_c^2}{2}Cos(2\omega_o t + \theta_{h_2}) + \frac{M_1 V_c^1}{4}Cos(2\omega_o t + \theta_{h_1}) - \frac{M_3 V_c^1}{4}Cos(2\omega_o t - \theta_{h_1}) + \frac{M_3 V_c^0}{2}Cos(3\omega_o t)$$
$$-\frac{M_1 V_c^2}{4}Cos(3\omega_o t + \theta_{h_2}) - \frac{M_2 V_c^1}{4}Cos(3\omega_o t + \theta_2 + \theta_{h_1}) + \frac{M_2 V_c^2}{4}Cos(4\omega_o t + \theta_2 + \theta_{h_2}) - \frac{M_3 V_c^2}{4}Cos(4\omega_o t + \theta_{h_1}) + \frac{M_3 V_c^2}{4}Cos(5\omega_o t + \theta_{h_2})$$
$$+Re\sum_{m=1}^{\infty}\sum_{n=-\infty}^{\infty}\left(\left\{\sum_{i=\{0,1,2\}}\left[\sum_{\substack{u_1,u_2,u_3,\\K,H,Z}}\frac{V_c^i}{\pi m}\left\{\begin{array}{c}e^{-j(u_1\theta_{h_i}+u_2 H\theta_2+u_3 Z\pi)}J_K\left(mM_1\frac{\pi}{2}\right)J_H\left(mM_2\frac{\pi}{2}\right)J_Z\left(mM_3\frac{\pi}{2}\right).\\Sin\left((m+K+H+Z)\frac{\pi}{2}\right)\end{array}\right\}\right|_{\substack{n=u_1 i \pm u_2 2H + u_3 3Z}}\right]\right\}e^{-j\left(m\left(\omega_c t+\frac{2\pi}{N}(k-1)+\theta_{psc}\right)+n(\omega_o t+\pi)\right)}\right)$$

$$v_a^{l,k}(t) = \frac{V_c^0}{2} + \frac{M_1 V_c^1}{4}Cos(\theta_{h_1}) + \frac{M_2 V_c^2}{4}Cos(\theta_{h_2} - \theta_2) \tag{16b}$$
$$+\frac{M_1 V_c^0}{2}Cos(\omega_o t) + \frac{V_c^1}{2}Cos(\omega_o t + \theta_{h_1}) + \frac{M_1 V_c^2}{4}Cos(\omega_o t + \theta_{h_2}) + \frac{M_2 V_c^1}{4}Cos(\omega_o t + \theta_2 - \theta_{h_1}) - \frac{M_3 V_c^2}{4}Cos(\omega_o t - \theta_{h_2})$$
$$+\frac{M_2 V_c^0}{2}Cos(2\omega_o t + \theta_2) + \frac{V_c^2}{2}Cos(2\omega_o t + \theta_{h_2}) + \frac{M_1 V_c^1}{4}Cos(2\omega_o t + \theta_{h_1}) - \frac{M_3 V_c^1}{4}Cos(2\omega_o t - \theta_{h_1}) - \frac{M_3 V_c^0}{2}Cos(3\omega_o t)$$
$$+\frac{M_1 V_c^2}{4}Cos(3\omega_o t + \theta_{h_2}) + \frac{M_2 V_c^1}{4}Cos(3\omega_o t + \theta_2 + \theta_{h_1}) + \frac{M_2 V_c^2}{4}Cos(4\omega_o t + \theta_2 + \theta_{h_2}) - \frac{M_3 V_c^1}{4}Cos(4\omega_o t + \theta_{h_1}) - \frac{M_3 V_c^2}{4}Cos(5\omega_o t + \theta_{h_2})$$
$$+Re\sum_{m=1}^{\infty}\sum_{n=-\infty}^{\infty}\left(\left\{\sum_{i=\{0,1,2\}}\left[\sum_{\substack{u_1,u_2,u_3,\\K,H,Z}}\frac{V_c^i}{\pi m}\left\{\begin{array}{c}e^{-j(u_1\theta_{h_i}+u_2 H\theta_2+u_3 Z\pi)}J_K\left(mM_1\frac{\pi}{2}\right)J_H\left(mM_2\frac{\pi}{2}\right)J_Z\left(mM_3\frac{\pi}{2}\right).\\Sin\left((m+K+H+Z)\frac{\pi}{2}\right)\end{array}\right\}\right|_{\substack{n=u_1 i \pm u_2 2H + u_3 3Z}}\right]\right\}e^{-j\left(m\left(\omega_c t+\frac{2\pi}{N}(k-1)\right)+n\omega_o t\right)}\right)$$
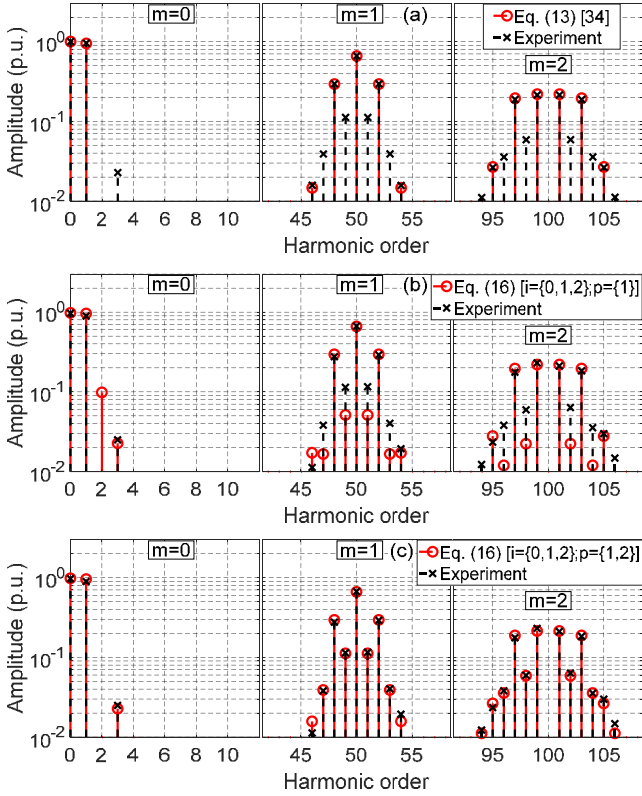
Fig. 9. Experimental results for Case-A – MMC SM ac voltage harmonic spectrum $v_a^{u,1}$ (a) Eq. (13) [34]. (b) Eq. (16) [i={0,1,2}; p={1}]. (c) Eq. (16) [i={0,1,2}; p={1,2}].

modulation signal and the first and second harmonics in the capacitor voltage, resulting in the new harmonics of the order

$(n = 1 \pm i)$ and $(n = i)$. The analytical prediction of the third harmonic is in good agreement with the experiment. However, no second harmonic has been found in the experimental results. The analytical predictions of the high frequency range are also improved with respect to the analytical harmonic spectrum (13) [34] shown in Fig. 9(a). The odd sideband harmonics in the first carrier group and the even sideband harmonics in the second carrier group are due to the first harmonic in the capacitor voltage. In general, the harmonics in the capacitor voltage will cause the sideband harmonics of the order $(n = \pm i \pm K)$ where $(K = 0,2,4 \dots)$ in the odd carrier groups, and the sidebands harmonics of the order $(n = \pm i \pm K)$ where $(K = 0,1,3 \dots)$ in the even carrier groups. Fig.9(c) shows the analytical harmonic spectrum (16) in which variables i and p are set as $i = \{0,1,2\}$ and $p = \{1,2\}$; namely, in this case the second order harmonic component in the modulation signal is also included. The amplitude and phase of the second harmonic in the modulation signal are obtained from the experiment. This harmonic is injected in the modulation signal by the closed control loop to regulate the second harmonic circulating current to zero [31]. The second harmonic component in the modulation signal will then eliminate the second order baseband harmonic in the harmonic spectrum, as is shown in Fig.9(c). The second harmonic component in the modulation signal also affects the sideband harmonics in the spectrum, as can be seen by comparing Fig.9(c) and Fig.9(b). The analytical results in Fig.9(c) are in excellent agreement with the experiment.

The experimental results of the arm voltage harmonic spectrum for Case A are compared with the analytical solutions (14) [34] and (17) in Fig.10. As expected, the first sidebands of the spectrum are centered about Nf_c, i.e. the first harmonic

$$v_a^u(t) = \frac{NV_c^0}{2} + \frac{NM_1V_c^1}{4}Cos(\theta_{h_1}) + \frac{NM_2V_c^2}{4}Cos(\theta_{h_2} - \theta_2) \tag{17a}$$

$$-\frac{NM_1V_c^0}{2}Cos(\omega_o t) - \frac{NV_c^1}{2}Cos(\omega_o t + \theta_{h_1}) - \frac{NM_2V_c^2}{4}Cos(\omega_o t + \theta_{h_2}) - \frac{NM_2V_c^1}{4}Cos(\omega_o t + \theta_2 - \theta_{h_1}) + \frac{NM_3V_c^2}{4}Cos(\omega_o t - \theta_{h_2})$$

$$+\frac{NM_2V_c^0}{2}Cos(2\omega_o t + \theta_2) + \frac{NV_c^2}{2}Cos(2\omega_o t + \theta_{h_2}) + \frac{NM_1V_c^1}{4}Cos(2\omega_o t + \theta_{h_1}) - \frac{NM_3V_c^1}{4}Cos(2\omega_o t - \theta_{h_1}) + \frac{NM_3V_c^0}{2}Cos(3\omega_o t)$$

$$-\frac{NM_1V_c^2}{4}Cos(3\omega_o t + \theta_{h_2}) - \frac{NM_2V_c^1}{4}Cos(3\omega_o t + \theta_2 + \theta_{h_1}) + \frac{NM_2V_c^2}{4}Cos(4\omega_o t + \theta_2 + \theta_{h_2}) - \frac{NM_3V_c^1}{4}Cos(4\omega_o t + \theta_{h_1}) + \frac{NM_3V_c^2}{4}Cos(5\omega_o t + \theta_{h_2})$$

$$+Re\sum_{m=1}^{\infty}\sum_{n=-\infty}^{\infty}\left(\left\{\sum_{i=\{0,1,2\}}\left[\sum_{\substack{u_1,u_2,u_3,\\K,H,Z}}\frac{V_c^i}{\pi m}\left\{\begin{matrix}e^{-j(u_1\theta_{h_i}+u_2H\theta_2+u_3Z\pi)}J_K\left(mNM_1\frac{\pi}{2}\right)J_H\left(mNM_2\frac{\pi}{2}\right)J_Z\left(mNM_3\frac{\pi}{2}\right)\cdot\\ Sin\left((mN+K+H+Z)\frac{\pi}{2}\right)\end{matrix}\right\}\right|_{n=u_1i\pm K+u_22H+u_33Z}\right]\right\}e^{-j(mN(\omega_c t+\theta_{psc})+n(\omega_o t+\pi))}\right)$$

$$v_a^l(t) = \frac{NV_c^0}{2} + \frac{NM_1V_c^1}{4}Cos(\theta_{h_1}) + \frac{NM_2V_c^2}{4}Cos(\theta_{h_2} - \theta_2) \tag{17a}$$

$$+\frac{NM_1V_c^0}{2}Cos(\omega_o t) + \frac{NV_c^1}{2}Cos(\omega_o t + \theta_{h_1}) + \frac{NM_2V_c^2}{4}Cos(\omega_o t + \theta_{h_2}) + \frac{NM_2V_c^1}{4}Cos(\omega_o t + \theta_2 - \theta_{h_1}) - \frac{NM_3V_c^2}{4}Cos(\omega_o t - \theta_{h_2})$$

$$+\frac{NM_2V_c^0}{2}Cos(2\omega_o t + \theta_2) + \frac{NV_c^2}{2}Cos(2\omega_o t + \theta_{h_2}) + \frac{NM_1V_c^1}{4}Cos(2\omega_o t + \theta_{h_1}) - \frac{NM_3V_c^1}{4}Cos(2\omega_o t - \theta_{h_1}) - \frac{NM_3V_c^0}{2}Cos(3\omega_o t)$$

$$+\frac{NM_1V_c^2}{4}Cos(3\omega_o t + \theta_{h_2}) + \frac{NM_2V_c^1}{4}Cos(3\omega_o t + \theta_2 + \theta_{h_1}) + \frac{NM_2V_c^2}{4}Cos(4\omega_o t + \theta_2 + \theta_{h_2}) - \frac{NM_3V_c^1}{4}Cos(4\omega_o t + \theta_{h_1}) - \frac{NM_3V_c^2}{4}Cos(5\omega_o t + \theta_{h_2})$$

$$+Re\sum_{m=1}^{\infty}\sum_{n=-\infty}^{\infty}\left(\left\{\sum_{i=\{0,1,2\}}\left[\sum_{\substack{u_1,u_2,u_3,\\K,H,Z}}\frac{V_c^i}{\pi m}\left\{\begin{matrix}e^{-j(u_1\theta_{h_i}+u_2H\theta_2+u_3Z\pi)}J_K\left(mNM_1\frac{\pi}{2}\right)J_H\left(mNM_2\frac{\pi}{2}\right)J_Z\left(mNM_3\frac{\pi}{2}\right)\cdot\\ Sin\left((mN+K+H+Z)\frac{\pi}{2}\right)\end{matrix}\right\}\right|_{n=u_1i\pm K+u_22H+u_33Z}\right]\right\}e^{-j(m\omega_c t+n\omega_o t)}\right)$$
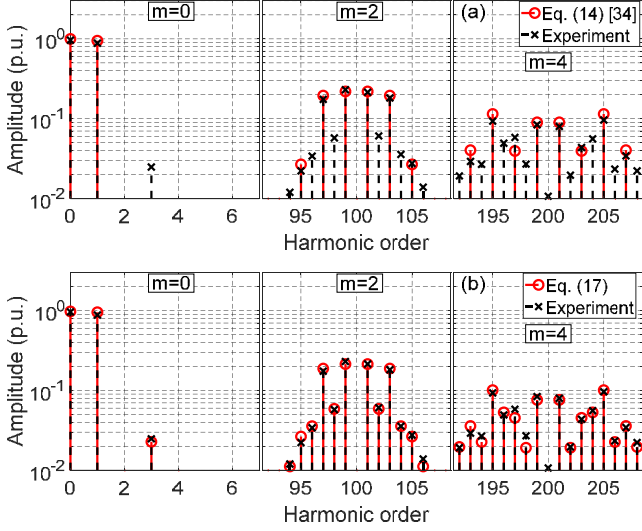
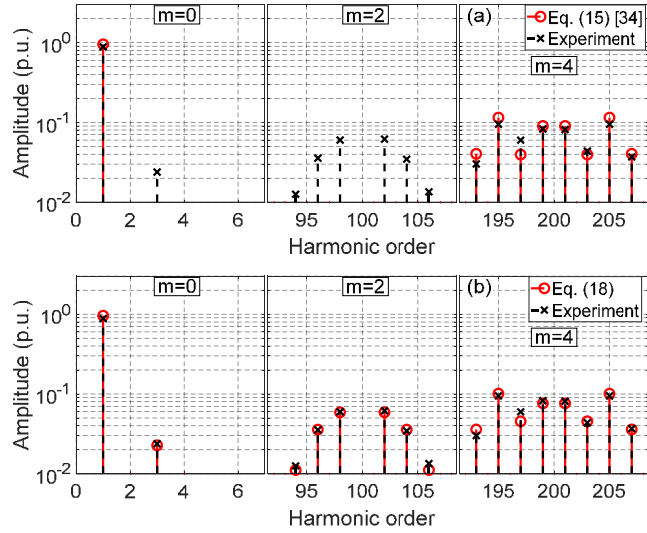Fig. 10. Experimental results for Case-A – MMC SM arm voltage harmonic spectrum v_a^u (a) Eq. (14) [34]. (b) Eq. (17).

Fig. 11. Experimental results for Case-A – MMC SM ac output voltage harmonic spectrum v_{ao}^- (a) Eq. (15) [34]. (b) Eq. (18).

Fig. 12. Experimental results for Case-B – MMC SM ac voltage harmonic spectrum $v_a^{u,1}$ (a) Eq. (13) [34]. (b) Eq. (16) [i={0,1,2}; p={1}]. (c) Eq. (16) [i={0,1,2}; p={1,2,3}].

group is given by ($m = 2$). The solution (17) is in excellent agreement with the experimental results, while the additional sidebands in the first and second carrier groups are not predicted by the solution (14). Finally, the experimentally results of the output voltage harmonic spectrum for Case A are compared with solutions (15) [34] and (18) in Fig.11. Instead of measuring the output voltage directly, the two arm voltages are
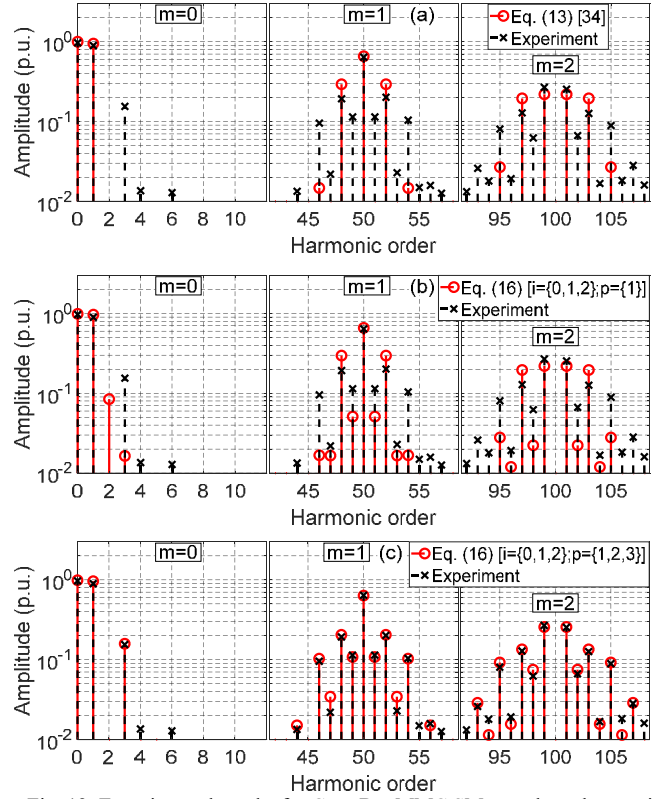
measured and the output voltage is obtained as $v_{ao}^- = (v_a^l - v_a^u)/2$. This is done to omit the effects of the arm inductors on the spectrum, as not accounted for in the analytical solutions. With the displacement angle between the upper and lower arms of $\theta_{psc} = \pi/2$ (with $N = 2$), one would expect the first sideband harmonics about $2Nf_c$, i.e. the first harmonic group given by ($m = 4$). [34]. However, due to the first and second order harmonics in the capacitor voltages and the second order harmonic component in the modulation signal, the full cancellation cannot be achieved for the harmonics in the harmonic group $m = 2$. These observations are important concerning the output filter design and will be discuss further in Section V. The new solution (18) can predict these effects and is in excellent agreement with the experimental results.

The experimental results for Case B (with the third harmonic injection PWM) are shown in Fig.12. The results are presented for the harmonic spectrum of the SM output voltage. Fig. 12(a)

$$v_a^u(t) = \frac{NM_1 V_c^0}{2} Cos(\omega_o t) + \frac{NV_c^1}{2} Cos(\omega_o t + \theta_{h_1}) + \frac{NM_1 V_c^2}{4} Cos(\omega_o t + \theta_{h_2}) + \frac{NM_2 V_c^1}{4} Cos(\omega_o t + \theta_2 - \theta_{h_1}) - \frac{NM_3 V_c^2}{4} Cos(\omega_o t - \theta_{h_2}) \quad (18)$$

$$- \frac{NM_3 V_c^0}{2} Cos(3\omega_o t) + \frac{NM_1 V_c^2}{4} Cos(3\omega_o t + \theta_{h_2}) + \frac{NM_2 V_c^1}{4} Cos(3\omega_o t + \theta_2 + \theta_{h_1}) - \frac{NM_3 V_c^2}{4} Cos(5\omega_o t + \theta_{h_2})$$

$$+ Re \sum_{m=1}^{\infty} \sum_{n=-\infty}^{\infty} \left(\left\{ \sum_{i=\{0,1,2\}} \left[\sum_{\substack{u_1,u_2,u_3, \\ K,H,Z}} \frac{V_c^i}{\pi m} \left\{ \begin{matrix} e^{-j(u_1\theta_{h_i}+u_2 H\theta_2+u_3 Z\pi)} J_K\left(mNM_1 \frac{\pi}{2}\right) J_H\left(mNM_2 \frac{\pi}{2}\right) \cdot \\ J_Z\left(mNM_3 \frac{\pi}{2}\right) Sin\left((mN+K+H+Z)\frac{\pi}{2}\right) \end{matrix} \right\} \right]_{n=u_1 i \pm K + u_2 2H + u_3 3Z} \right\} e^{-j(m\omega_c t + n\omega_o t)} \left(\frac{1 - e^{-j(mN\theta_{psc}+n\pi)}}{2} \right) \right)$$

clearly shows that solution (13) [34] has failed to identify the odd sidebands in the first carrier group and the even sidebands in the second carrier group, and the dominant third baseband harmonic. The solution (16) with $i = \{0,1,2\}$ and $p = \{1\}$, shown in Fig.12(b), is in better agreement with the experiment, as it identifies the additional sidebands which are caused by the capacitor voltage harmonics. In Fig.12(c), the analytical solution (16), with $i = \{0,1,2\}$ and $p = \{1,2,3\}$, which also captures the effects of the third and second order harmonics in the modulation signal, is in good agreement with the experiment.

V. EFFECT OF SM CAPACITANCE ON OUTPUT FILTER DESIGN

To understand the effect of the SM capacitor voltage ripple on the MMC output voltage quality Total Harmonic Distortion (THD) and Weighted THD (WTHD) [7] are examined in this section through simulations. The same system parameters as in the experimental setup in Section IV are used for this analysis. The block diagram of the simulation model is shown in Fig.13. The output filter at the converter terminals is formed by the arm inductor L_b (where $L_f = L_b/2$) and the shunt capacitor C_f.

Fig.14 shows THD and WTHD of the MMC output voltage before the filter is connected for the set of different SM capacitances. The corresponding variations in the SM capacitor voltage ripple (denoted as ΔV_C) are also included in Fig.14. It can be seen that for the capacitor voltage ripple above 15%, WTHD starts increasing, while THD is not affected. WTHD is however a better measure of the output voltage quality as it accounts for the order of each harmonic component.

Fig.15(a) and Fig.15(b) show the output voltage before and after the filter is connected, with THD of 30.88% and 4%, respectively. The SM capacitance in this case was $C = 500\mu F$. Further, in order to demonstrate the output filter requirements, the inductance L_f is assumed constant ($L_f = L_b/2$) and the capacitance C_f and resistance R_f are varied to keep the output voltage THD constant at ~4% for the different SM capacitance values and the results are shown in Fig.16. It is clear that as the SM capacitance is decreased the filter size is increased which can be seen by the increase in the required filter capacitance C_f. The filter cut-off frequency, which relates to the filter size (as lower cut-off frequency results in the larger filter [21]) and is given by $f_{cu} = 1/2\pi\sqrt{C_f L_f}$, is also shown in Fig. 16 to further demonstrate the filter requirements.

VI. CONCLUSION

The new analytical solution to the output voltage harmonic spectrum of the single phase inverter developed in this work is applicable to a wide variety of power converters operated with non-ideal dc-bus voltage. The study shows that when the dc-bus voltage is non-ideal the additional harmonic components are introduced in the spectrum. In general, for a sinusoidal modulation signal, the ith order harmonic in the dc bus voltage will generate the baseband harmonics of the order $n = i$ and $n =$
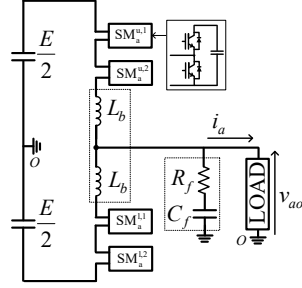

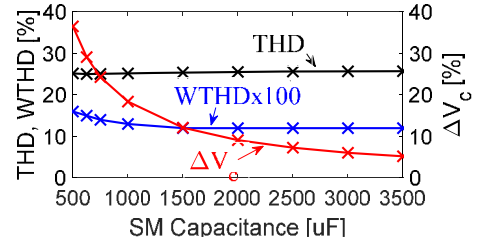Fig. 13. MMC with output voltage filter.

Fig. 14. MMC output voltage THD versus SM capacitance.
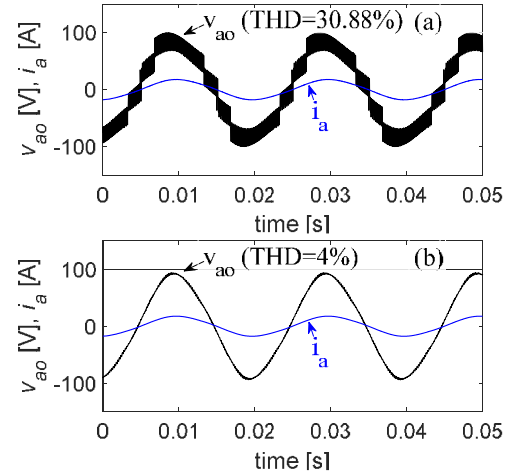

Fig. 15. Output voltage v_{ao} and current i_a waveforms. (a) without LC filter. (b) with LC filter.
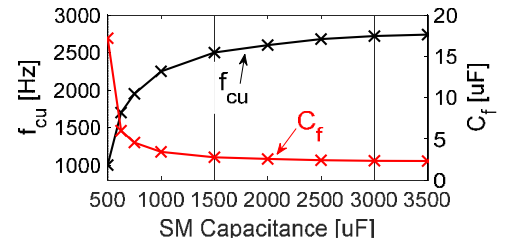
Fig. 16. Variation in filter capacitance C_f and filter cut-off frequency f_{cu} for different SM capacitance values.

$\|1 \pm i\|$. Also, it will generate the carrier and sideband harmonics of the order $n = (\pm i \pm K)$ with $K = (0, 2, 4, \dots)$ for the odd carrier groups and $K = (1, 3, 5, \dots)$ for the even carrier groups. The amplitudes of these harmonics depend on the amplitude and the relative phase shift angle of the dc bus voltage harmonics. The study has also included the more complex problem when the modulation signal includes

fundamental and baseband components. In general, the ith order harmonic component in the dc bus voltage and the fundamental and the pth order harmonic components in the modulation signal will generate the baseband harmonics of the order $n = i$, $n = \|1 \pm i\|$, $n = \|p \pm i\|$) and the carrier and sideband harmonics of the order $n = (\pm i \pm K \pm pH)$ for $(m + K + H)$ is odd, where m represents multiples of the carrier frequency and $0 \leq K \leq \infty$, $0 \leq H \leq \infty$.

Further, as the single phase inverter forms the basic building block of the MMCs, and starting from the general solution, the new solution to the MMC output voltage harmonic spectrum is also developed in this work. The MMC harmonic solution is developed for the PSCPWM and can include the effects of the closed loop circulating current control and the third harmonic injection in the modulation signal. The low-capacitance MMC is chosen in this analysis due to inherent low-frequency voltage oscillations in the converter internal capacitors.

The study reveals that, as the new sideband harmonics are present in the spectrum, due to the interactions between the dc bus voltage harmonics and the fundamental and baseband components in the modulation signal, the sidebands centered about Nf_c (where N is the number of SMs per arm and f_c is the SM frequency) in the arm voltages, will not be cancelled in the output voltage, as would be expected for ideal SM capacitor voltages. Therefore the first sideband harmonics in the MMC output voltage will be centered about Nf_c instead of $2Nf_c$. This results in an increase in the output voltage WTHD and consequently the size of the output filter.

APPENDIX

The harmonic spectrum of a general carrier-based PWM waveform can be expressed by:

$$f(t) = \frac{C_{00}}{2} + Re \sum_{n=1}^{\infty} C_{0,n} e^{-jny} + Re \sum_{m=1}^{\infty} \sum_{n=-\infty}^{n=\infty} C_{m,n} e^{-j(mz+ny)} \tag{A0a}$$

where the coefficients are defined as:

$$C_{m,n} = \frac{1}{2\pi^2} \int_{-\pi}^{\pi} \int_{-\pi}^{\pi} f(z,y) e^{j(mz+ny)} dz\, dy \tag{A0b}$$

where Re indicates the real part of the complex quantity.

In particular, the coefficients $C_{m,n}$ for the multi-frequency modulation signal (9) and the capacitor voltage (5) are given by (A1a) where the coefficients $C_{m,n}^i$ are defined by (A1b) and the solution (10) can be obtained.

REFERENCES

[1] "IEEE Recommended Practice for Monitoring Electric Power Quality," *IEEE Std 1159-2009 (Revision of IEEE Std 1159-1995)*. pp. c1-81, 2009.

[2] T. J. Browne and G. T. Heydt, "Power Quality as an Educational Opportunity," *IEEE Trans. Power Syst.*, vol. 23, no. 2, pp. 814–815, 2008.

[3] W. R. Bennett, "New results in the calculation of modulation products," *Bell Syst. Tech. J.*, vol. 12, no. 2, pp. 228–243, 1933.

[4] H. S. Black, *Modulation Theory*. New York: Van Nostrand, 1953.

[5] S. R. Bowes, "New sinusoidal pulse width-modulated inverter," *Proc. Inst. Elect. Eng.*, vol. 122, no. 11, pp. 1279–1285, Nov. 1975.

[6] A. M. Hava, R. J. Kerkman, and T. A. Lipo, "Simple analytical and graphical methods for carrier-based PWM-VSI drives," *IEEE Trans. Power Electron.*, vol. 14, no. 1, pp. 49–61, 1999.

[7] D. G. Holmes and T. A. Lipo, *Pulse Width Modulation of Power Converters: Principles and Practice*. Piscataway, NJ: Wiley-IEEE Press, 2003.

[8] M. Odavic, M. Sumner, P. Zanchetta, and J. C. Clare, "A Theoretical Analysis of the Harmonic Content of PWM Waveforms for Multiple-Frequency Modulators," *IEEE Trans. Power Electron.*, vol. 25, no. 1, pp. 131–141, 2010.

[9] D. C. Moore, M. Odavic, and S. M. Cox, "Dead-time effects on the voltage spectrum of a PWM inverter," *IMA J. Appl. Math.*, vol. 79, no. 6, pp. 1061–1076, Dec. 2014.

[10] C. M. Wu, W.-H. Lau, and H. S.-H. Chung, "Analytical technique for calculating the output harmonics of an H-bridge inverter with dead time," *IEEE Trans. Circuits Syst. I Fundam. Theory Appl.*, vol. 46, no. 5, pp. 617–627, 1999.

[11] F. Chierchie, L. Stefanazzi, E. E. Paolini, and A. R. Oliva, "Frequency Analysis of PWM Inverters With Dead-Time for Arbitrary Modulating Signals," *IEEE Trans. Power Electron.*, vol. 29, no. 6, pp. 2850–2860, 2014.

[12] I. Dolguntseva, R. Krishna, D. E. Soman, and M. Leijon, "Contour-Based Dead-Time Harmonic Analysis in a Three-Level Neutral-Point-Clamped Inverter," *IEEE Trans. Ind. Electron.*, vol. 62, no. 1, pp. 203–210, 2015.

[13] H. d. T. Mouton, B. McGrath, D. G. Holmes, and R. H. Wilkinson, "One-Dimensional Spectral Analysis of Complex PWM Waveforms Using Superposition," *IEEE Trans. Power Electron.*, vol. 29, no. 12, pp. 6762–6778, 2014.

[14] H. Mouton and B. Putzeys, "Understanding the PWM Nonlinearity: Single-Sided Modulation," *IEEE Trans. Power Electron.*, vol. 27, no. 4, pp. 2116–2128, 2012.

[15] D. J. Kostic, Z. Z. Avramovic, and N. T. Ciric, "A New Approach to Theoretical Analysis of Harmonic Content of PWM Waveforms of Single- and Multiple-Frequency Modulators," *IEEE Trans. Power Electron.*, vol. 28, no. 10, pp. 4557–4567, 2013.

[16] S. Debnath, J. Qin, B. Bahrani, M. Saeedifard, and P. Barbosa, "Operation, control, and applications of the modular multilevel converter: A review," *IEEE Trans. Power Electron.*, vol. 30, no. 1, pp. 37–53, Jan. 2015.

[17] J. Kolb, F. Kammerer, and M. Braun, "Dimensioning and design of a modular multilevel converter for drive applications," in *15th International Power Electronics and Motion Control Conference and Exposition, EPE-PEMC 2012 ECCE Europe*, Novi Sad, Europe, 2012, pp. LS1a-1.1-1-LS1a-1.1-8.

[18] K. Ilves, S. Member, A. Antonopoulos, S. Member, and S. Norrga, "Steady-State Analysis of Interaction Between Harmonic Components of Arm and Line Quantities of MMC," *IEEE Trans. Power Electron.*, vol. 27, no. 1, pp. 57–68, 2012.

[19] R. Oliveira and A. Yazdani, "An Enhanced Steady-State Model and Capacitor Sizing Method for Modular Multilevel Converters for HVdc Applications," *IEEE Trans. Power Electron.*, vol. 33, no. 6, pp. 4756–4771, Jun. 2018.

[20] Q. Song, W. Liu, X. Li, H. Rao, S. Xu, and L. Li, "A steady-state analysis method for a modular multilevel converter," *IEEE Trans. Power Electron.*, vol. 28, no. 8, pp. 3702–3713, 2013.

[21] F. Deng, Z. Chen, D. Karwatzki, A. Mertens, M. Parker, and S. Finney, "Converter designs based on new components and modular multilevel

$$C_{m,n} = C_{m,n}^0 + C_{m,n}^{i_1} + C_{m,n}^{i_2} + \cdots = \sum_{i \in I} C_{m,n}^i \tag{A1a}$$

$$C_{m,n}^i = \frac{1}{2\pi^2} \int_{-\pi}^{\pi} \int_{-\frac{\pi}{2}(1+M_1 Cosy + M_{p_2}\cos(p_2 y + \theta_{p_2}) + M_{p_3}\cos(p_3 y + \theta_{p_3}))}^{\frac{\pi}{2}(1+M_1 Cosy + +M_{p_2}\cos(p_2 y + \theta_{p_2}) + M_{p_3}\cos(p_3 y + \theta_{p_3}))} V_c^i Cos(iy + \theta_{h_i}) e^{j(mz+ny)} dz\, dy \tag{A1b}$$

topologies," *Innovative Wind Conversion Systems (INNWIND.EU)*, Europe, Tech. Report, Nov. 2017.

[22] Q. Song, W. Yang, B. Zhao, J. Meng, S. Xu, and Z. Zhu, "Low-Capacitance Modular Multilevel Converter Operating With High Capacitor Voltage Ripples," *IEEE Trans. Ind. Electron.*, vol. 66, no. 10, pp. 7456–7467, 2019.

[23] G. Farivar, C. D. Townsend, B. Hredzak, J. Pou, and V. G. Agelidis, "Low-Capacitance Cascaded H-Bridge Multilevel StatCom," *IEEE Trans. Power Electron.*, vol. 32, no. 3, pp. 1744–1754, 2017.

[24] G. Farivar, B. Hredzak, and V. G. Agelidis, "Reduced-Capacitance Thin-Film H-Bridge Multilevel STATCOM Control Utilizing an Analytic Filtering Scheme," *IEEE Trans. Ind. Electron.*, vol. 62, no. 10, pp. 6457–6468, 2015.

[25] T. Isobe, D. Shiojima, K. Kato, Y. R. R. Hernandez, and R. Shimada, "Full-Bridge Reactive Power Compensator With Minimized-Equipped Capacitor and Its Application to Static Var Compensator," *IEEE Trans. Power Electron.*, vol. 31, no. 1, pp. 224–234, 2016.

[26] K. Ilves, S. Norrga, L. Harnefors, and H. Nee, "On Energy Storage Requirements in Modular Multilevel Converters," *IEEE Trans. Power Electron.*, vol. 29, no. 1, pp. 77–88, 2014.

[27] Y. Tang, L. Ran, O. Alatise, and P. Mawby, "Capacitor Selection for Modular Multilevel Converter," *IEEE Trans. Ind. Appl.*, vol. 52, no. 4, pp. 3279–3293, 2016.

[28] S. Kouro, P. Lezana, M. Angulo, and J. Rodriguez, "Multicarrier PWM With DC-Link Ripple Feedforward Compensation for Multilevel Inverters," *IEEE Trans. Power Electron.*, vol. 23, no. 1, pp. 52–59, 2008.

[29] C. D. Townsend, T. J. Summers, and R. E. Betz, "Impact of Practical Issues on the Harmonic Performance of Phase-Shifted Modulation Strategies for a Cascaded H-Bridge StatCom," *IEEE Trans. Ind. Electron.*, vol. 61, no. 6, pp. 2655–2664, 2014.

[30] M. Huang, J. Zou, and X. Ma, "An Improved Phase-Shifted Carrier Modulation for Modular Multilevel Converter to Suppress the Influence of Fluctuation of Capacitor Voltage," *IEEE Trans. Power Electron.*, vol. 31, no. 10, pp. 7404–7416, 2016.

[31] X. Li, Q. Song, W. Liu, S. Xu, Z. Zhu, and X. Li, "Performance Analysis and Optimization of Circulating Current Control for Modular Multilevel Converter," *IEEE Trans. Ind. Electron.*, vol. 63, no. 2, pp. 716–727, 2016.

[32] S. P. Engel and R. W. De Doncker, "Control of the Modular Multi-Level Converter for minimized cell capacitance," in *Proc. European Conference on Power Electronics and Applications*, Birmingham, UK, 2011, pp. 1–10.

[33] M. Hagiwara, I. Hasegawa, and H. Akagi, "Start-Up and Low-Speed Operation of an Electric Motor Driven by a Modular Multilevel Cascade Inverter," *IEEE Trans. Ind. Appl.*, vol. 49, no. 4, pp. 1556–1565, 2013.

[34] B. Li, R. Yang, D. Xu, G. Wang, W. Wang, and D. Xu, "Analysis of the phase-shifted carrier modulation for modular multilevel converters," *IEEE Trans. Power Electron.*, vol. 30, no. 1, pp. 297–310, 2015.

[35] Y. Li, Y. Wang, and B. Q. Li, "Generalized Theory of Phase-Shifted Carrier PWM for Cascaded H-Bridge Converters and Modular Multilevel Converters," *IEEE J. Emerg. Sel. Top. Power Electron.*, vol. 4, no. 2, pp. 589–605, 2016.

[36] J. Wang, J. Liang, F. Gao, X. Dong, C. Wang, and B. Zhao, "A Closed-Loop Time-Domain Analysis Method for Modular Multilevel Converter," *IEEE Trans. Power Electron.*, vol. 32, no. 10, pp. 7494–7508, 2017.

[37] L. Angquist, A. Antonopoulos, D. Siemaszko, K. Ilves, M. Vasiladiotis, and H. Nee, "Open-Loop Control of Modular Multilevel Converters Using Estimation of Stored Energy," *IEEE Trans. Ind. Appl.*, vol. 47, no. 6, pp. 2516–2524, 2011.

[38] M. Hagiwara and H. Akagi, "Control and Experiment of Pulsewidth-Modulated Modular Multilevel Converters," *IEEE Trans. Power Electron.*, vol. 24, no. 7, pp. 1737–1746, 2009.

[39] N. Thitichaiworakorn, M. Hagiwara, and H. Akagi, "Experimental Verification of a Modular Multilevel Cascaded Inverter Based on Double-Star Bridge Cells," *IEEE Trans. Ind. Appl.*, vol. 50, no. 1, pp. 509–519, 2014.

[40] Z. Li, P. Wang, Z. Chu, H. Zhu, Y. Luo, and Y. Li, "An Inner Current Suppressing Method for Modular Multilevel Converters," *IEEE Trans. Power Electron.*, vol. 28, no. 11, pp. 4873–4879, 2013.